High-energy electron radiography system with low chromatic aberrations based on active plasma lenses

Jie-Jie Lan,[1] Quan-Tang Zhao,[2,3,*] Zhang-Hu Hu,[1,†] Zhao-Hui Ran,[2] Wang-Wen Xu,[1] Hao-Yuan Li,[1] Jia Li,[2] Shu-Chun Cao,[2,3] Rui Cheng,[2] Yong-Tao Zhao,[4] Zi-Min Zhang,[2,3] and You-Nian Wang[1]

[1] *School of Physics, Dalian University of Technology, Dalian 116024, People's Republic of China*
[2] *Institute of Modern Physics, Chinese Academy of Sciences, Lanzhou 730000, People's Republic of China*
[3] *School of Nuclear Science and Technology, University of Chinese Academy of Sciences, Beijing 100049, People's Republic of China*
[4] *School of Physics, Xi'an Jiaotong University, Xi'an 710049, People's Republic of China*

(Received 15 April 2024; revised 25 July 2024; accepted 30 August 2024; published 10 September 2024)

A novel high-energy electron radiography system combined with an active plasma lens (APL) has been designed for the first time and validated by simulation studies. The system consists of a 50-MeV electron linear accelerator followed by a 3-cm-long capillary with a discharge current up to hundreds of amperes. With the APL, the distance from the object plane to the imaging plane can be reduced from 5 m to 45 cm with a magnification factor (MF) of 20, and pictures with 1.1-μm spatial resolution can be obtained. The effects of lens chromatic aberrations, imaging blurring, and the uniformity of the plasma discharge current are shown to be significant in obtaining a high-spatial-resolution radiograph, which have been discussed in this work. Such a plasma-based imaging lens has a high tolerance for chromatic aberrations, is suitable for imaging thick target materials, and has radial symmetric focusing and adjustable focusing gradients. Furthermore, a cascaded high-MF radiography system based on APLs has been proposed to improve spatial resolution.

DOI: 10.1103/PhysRevApplied.22.034022

I. INTRODUCTION

Driven by the diagnostics of high-energy-density materials, lens-focused charged-particle radiography has been developed at the Los Alamos Nuclear Science Center [1] with 800-MeV protons for dynamic experiments. As an alternative to proton radiography, high-energy electron radiography (HEER) [2,3] has attracted considerable interest owing to its high spatial and temporal resolutions, large penetration depth, and low cost. A portable 30-MeV electron source and radiography system were first designed and built at Los Alamos National Laboratory with a spatial resolution of ∼100 μm and a time scale of microseconds [2]. Further, the HEER experiment with a picosecond pulse width has been achieved through the cooperation between the Institute of Modern Physics (IMP), the Chinese Academy of Sciences, and Tsinghua University [4]. So far, the spatial resolution of HEER has been improved to a few microns [5–7], and the time-resolved imaging of dynamic processes in a pump-probe scheme can reach the picosecond scale in a photoinjector [8].

The high spatial resolution of the HEER system can be achieved with a lens system. One option for the imaging lens would be using conventional focusing systems, such as solenoids [9], electromagnetic quadrupole magnets [4,6], and permanent magnet quadrupoles (PMQs) [8,10]. A solenoid that focuses beams in both horizontal and vertical directions is only suitable for electron beams in low-energy sections of a few mega-electron-volts or less. The electromagnetic quadrupole with an adjustable magnetic gradient must be used in groups. PMQs are usually chosen as the magnetic focusing elements because of their high gradients (one to two orders of magnitude higher than electromagnetic quadrupoles, up to ∼500 T/m [11]), low cost, and simplicity of operation compared to electromagnets. However, since the gradient of PMQs cannot be tuned, the positions of these PMQs should be optimized [10].

Plasma-based lenses [12–15] have been widely used in plasma accelerators for the advantages of compact, axisymmetric focusing, and high focusing gradients. Moreover, the development of plasma lenses could be a key technology for future e^+e^- linear colliders [16,17], potentially enabling higher-energy collisions and more compact facilities. By passing a strong current through the

*Contact author: zhaoquantang@impcas.ac.cn
†Contact author: zhanghu@dlut.edu.cn

discharge capillary, active plasma lenses (APLs) [12,13] can provide focusing fields up to kiloteslas per meter (kT/m), orders of magnitude stronger focusing compared to conventional focusing systems. It has been confirmed that, even at these very high gradients, APLs can remain linear throughout the time and aperture ranges with the discharge gas of argon [18]. In addition, the focusing gradient can be fine-tuned simply by changing the delay time of the discharge, without incurring nonlinearity [18]. Experimental observation of the electron beam focusing effect induced by plasma currents has been achieved at IMP [19]. At a delay time $\Delta t = 5.7\,\mu s$ after plasma ignition with a current $I_{pe} \approx 1\,kA$, the beam radius is reduced by a factor of 2.6 compared to the case of plasma discharge off.

Previous experimental studies [7] have shown that the length of the imaging lens system based on four magnetic quadrupoles with a magnification factor (MF) of 10 is 5 m. Additionally, an MF ∼15 with an overall length of 3 m has been obtained using high-gradient PMQs. In this work, we propose a HEER scheme design based on high-energy electron probes from conventional rf accelerators and a compact imaging lens composed of an APL. This lens has a weak chromatic dependence to realize a point-to-point focus. An MF of 20 can be obtained with a 50-MeV electron linear accelerator combined with a 3-cm-long capillary. In addition, the entire imaging columns magnify the sample in less than 45 cm.

This paper is organized as follows. The beam-plasma parameters of the imaging lens system and the corresponding proof-of-principle simulation results are presented in Sec. II. In Sec. III, we discuss the factors that affect spatial resolution, including the chromatic aberrations, the position and radius of the aperture, and the uniformity of the discharge current. Furthermore, we discuss the possibility of obtaining an even larger MF with a cascaded magnification system based on the APL. And, finally, we summarize the work in Sec. IV.

II. IMAGING LENS SYSTEM DESIGN AND SIMULATION

The HEER system is composed of three parts: the electron source, the matching segment (which is not discussed in this work), and the imaging lens system, as clearly illustrated in Fig. 1. The electron beam coming from the photocathode is then focused by a solenoid magnet. Downstream of the magnet is a 3-m-long accelerating cavity. At the exit of the accelerator cavity, four quadrupole electromagnets are used to focus the beam and match it to the imaging lens section. Then, the beam electrons passing through the target enter into the imaging lens and finally form a point-to-point image of the sample on the imaging plane. In general, the imaging lens system may be composed of electromagnetic quadrupole magnets or PMQs, or a combination of these magnets. In this work, a compact imaging lens system based on an APL is proposed.

A. High-energy electron beam

To obtain a high spatiotemporal resolution, especially in high-energy-density physics experiments, a state-of-the-art high-brightness electron source from an rf photoinjector is indispensable. The electron linear accelerator adopted in this HEER design has been developed at IMP. It consists of two different types of electron guns shown in Fig. 2: a thermionic cathode rf gun, which has been successfully used to radiograph thin static objects with root-mean-square (rms) spatial resolution of microns; and a photocathode rf gun, which is under construction for radiography of dynamic objects.

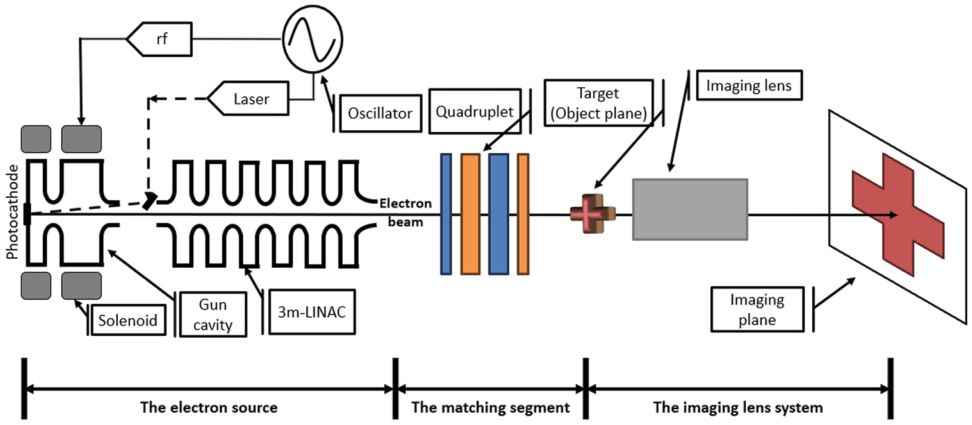

FIG. 1. Schematic of the HEER system (not to scale). It consists of a LINAC based on a photocathode injector (the electron source), the matching segment (four quadrupole electromagnets that are used to focus the beam and match it to the imaging lens section), and the imaging lens system. In general, the imaging lens system may be composed of electromagnetic quadrupole magnets or PMQs, or a combination of these magnets. In this work, a compact imaging lens system based on an APL is proposed, and proof-of-principle verification simulations for it are shown in Sec. II B.

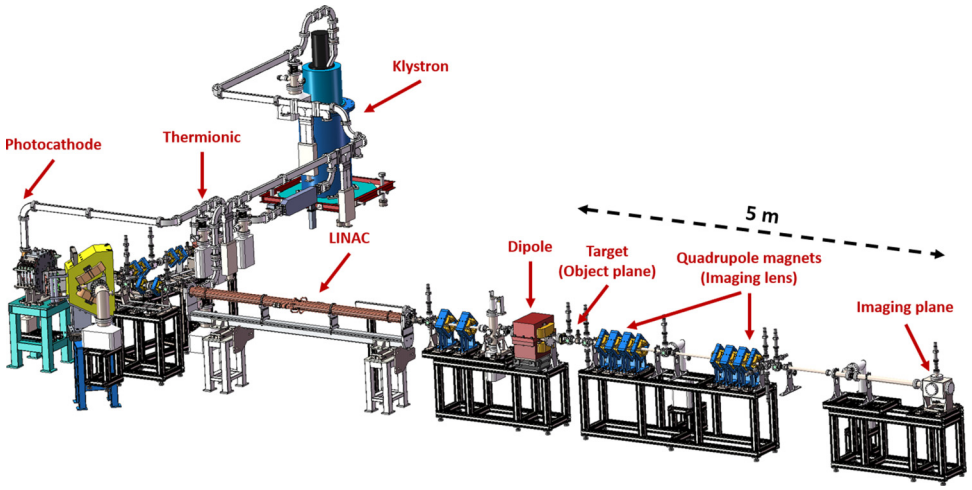

FIG. 2. The present layout of the HEER beamline at IMP with the imaging lens of quadrupoles. The length from the object plane to the imaging plane is 5 m, as shown. In this work, a compact imaging lens system based on an APL is used to reduce the length to 45 cm.

The present layout of the HEER beamline at IMP with the imaging lens of quadrupoles is shown in Fig. 2. The photocathode rf gun provides low emittance (1 mm mrad) and picosecond-pulse-width electron beams with energy of about 5 MeV. It should be noted that the low emittance is realized by using a solenoid at the exit of the rf gun, which is referred to as the emittance compensation process [20]. Then the beam enters into a 3-m-long S-band accelerating cavity, which operates at the $2\pi/3$ mode and with a maximum acceleration gradient of 22.5 MV/m [19]. At the end of the accelerating tube, an electron beam up to 50 MeV can be obtained.

For the HEER experiment design, an electron beam with energy of 50 MeV, spot size ∼1 mm, bunch charge 200 pC, emittance ∼1 mm mrad, energy spread ∼0.5%, and duration about 2 ps are chosen for stable running in the following. The pulse width, beam emittance, and energy spread are measured by the method of coherent transition radiation, quadruple scan method, and a dipole magnet (see Fig. 2), respectively. In this work, to form a compact point-to-point image design of the sample, an APL is adopted due to its ultrahigh gradient and axisymmetric focusing. With the APL, the distance from the object plane to the imaging plane can be compressed to 45 cm with an MF of 20, in contrast to 5 m in the case of quadrupole magnets with an MF of 10.18 in Fig. 2. The design of the imaging lens system and its working parameters are shown in Sec. II B.

B. System design and simulation results

A discharge capillary with a diameter of 1 mm, length of 3 cm, maximum plasma electron density of $n_{\mathrm{pe}} \sim 10^{22}$ m^{-3}, and discharge current up to ∼1 kA is adopted in the design. Numerous current trace measurements have been made for such a capillary, and a linear focusing magnetic field can be achieved in argon-filled APLs [18,21]. Therefore, it is reasonable to assume that the discharge current is uniformly distributed in the capillary with radius R. The magnetic field gradient can thus be calculated as a function of the radial position $r = \sqrt{x^2 + y^2}$ using Ampère's law [19,21]: $B_\theta = \mu_0 I_{\mathrm{pe}} r/(2\pi R^2) = gr$, with $g = \partial B_\theta/\partial r$ the magnetic field gradient, I_{pe} the discharge current, and μ_0 the permeability of vacuum. For the designed discharge capillary in this work with $I_{\mathrm{pe}} =$ 500 A and $R = 0.5$ mm, we have a magnetic field gradient $g = 400$ T/m. Furthermore, the peak beam density is about 2.8×10^{19} m^{-3} with the beam parameters discussed in Sec. II A. With the beam-plasma parameters mentioned above, the beam self-focusing effect can be neglected with the gradient being much smaller than that of the azimuthal magnetic field induced by the plasma discharge current [12,19], which has also been verified in simulations (not shown here).

As a first step, we derive the first-order transfer matrix of APLs, which is a simple way to design an imaging lens beamline. Considering the radial motions of the beam electron in the discharge capillary, the evolution of radial momentum satisfies $p_r' = -ecB_\theta$, where the prime is used to indicate a derivation with respect to t, such as $p_r' = dp_r/dt$, e is the electronic charge, and with the assumption that the electrons move along the direction of z with velocity $\sim c$.

By a proper transformation of the variables, however, we can express p_r' exactly in the form of the equation for a harmonic oscillator with constant frequency: $r'' = -\omega^2 r$, where $\omega = \sqrt{ec\mu_0 j_z/(2\gamma_0 m_{\mathrm{e}})}$ is the betatron frequency, with $j_z = I_{\mathrm{pe}}/\pi R^2$ the plasma current density, γ_0 the Lorentz factor of the beam, and m_{e} the electron rest mass. With $z = ct$, the evolution of the beam radius r with

the propagation distance z can be deduced:

$$r(z) = A_1 \sin\left(\frac{\omega}{c}z\right) + A_2 \cos\left(\frac{\omega}{c}z\right). \tag{1}$$

The coefficients A_1 and A_2 can be given by the initial radius and divergence angles of the electron beam, i.e., $A_1 = r'(0)/(\omega/c)$ and $A_2 = r(0)$. We then define a focusing strength parameter $K = \omega^2/c^2$ with reference to the quadrupole magnet.

Applying this to Eq. (1), the equations of motion for HEER systems based on an APL can be expressed as

$$\begin{aligned} r(z) &= \cos(\sqrt{K}z)r(0) + [\sin(\sqrt{K}z)/\sqrt{K}\,]r'(0), \\ r'(z) &= -\sqrt{K}\sin(\sqrt{K}z)r(0) + \cos(\sqrt{K}z)r'(0). \end{aligned} \tag{2}$$

Equation (2) can be expressed in matrix formulation as

$$\begin{bmatrix} r(z) \\ r'(z) \end{bmatrix} = \begin{bmatrix} \cos(\sqrt{K}L_2) & \sin(\sqrt{K}L_2)/\sqrt{K} \\ -\sqrt{K}\sin(\sqrt{K}L_2) & \cos(\sqrt{K}L_2) \end{bmatrix} \cdot \begin{bmatrix} r(0) \\ r'(0) \end{bmatrix}, \tag{3}$$

where

$$R_{\mathrm{APL}} = \begin{bmatrix} \cos(\sqrt{K}L_2) & \sin(\sqrt{K}L_2)/\sqrt{K} \\ -\sqrt{K}\sin(\sqrt{K}L_2) & \cos(\sqrt{K}L_2) \end{bmatrix}, \tag{4}$$

is the first-order transfer matrix of an APL, with L_2 the length of the discharge capillary, which is similar to that of the focusing quadrupole magnet.

Based on the first-order transfer matrices of the APL [Eq. (4)] and vacuum sections, the imaging lens system with an MF of 20 can be designed, as illustrated in Fig. 3. In this figure, beam electrons are set on the object plane with positions 0, ±250 μm, and ±475 μm and divergence angles of 0, ±9 mrad, and ±24 mrad, which are colored green, blue, red, black, and pink, respectively. The influences of the divergence angle as well as the beam offset on the performance of the plasma-based imaging lens are detailed in the Appendix. In addition, an aperture is placed on the Fourier plane, where the trajectories are radially sorted by scattering introduced at the object location. Note that the lens system must provide a point-to-point focus from the sample (i.e., the object plane) to the image plane, which can be conveniently expressed in the matrix formalism as

$$\begin{aligned} \begin{bmatrix} r(z) \\ r'(z) \end{bmatrix}_{\mathrm{image}} &= \begin{bmatrix} 1 & L_3 \\ 0 & 1 \end{bmatrix} \cdot R_{\mathrm{APL}} \cdot \begin{bmatrix} 1 & L_1 \\ 0 & 1 \end{bmatrix} \cdot \begin{bmatrix} r(0) \\ r'(0) \end{bmatrix} \\ &= R \cdot \begin{bmatrix} r(0) \\ r'(0) \end{bmatrix}, \end{aligned} \tag{5}$$

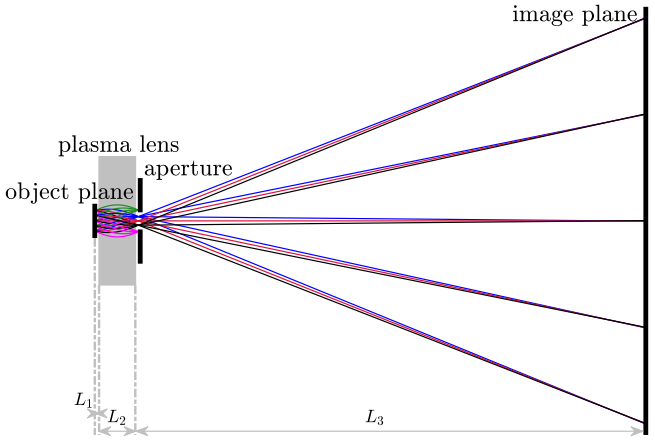

FIG. 3. Electron trajectories from the object plane to the image plane. Beam electrons are set on the object plane with positions 0, ±250 μm, and ±475 μm and divergence angles of 0, ±9 mrad, and ±24 mrad, which are colored green, blue, red, black, and pink, respectively. Here L_1 and L_3 are the lengths of the vacuum drift section and L_2 is the length of the plasma lens. In addition, an aperture is placed on the Fourier plane, where the trajectories are radially sorted by scattering introduced at the object location.

where

$$R = \begin{bmatrix} C - L_3\sqrt{K}S & L_1C + S/\sqrt{K} - L_1L_3\sqrt{K}S + L_3C \\ -\sqrt{K}S & -\sqrt{K}L_1S + C \end{bmatrix}, \tag{6}$$

with $C = \cos(\sqrt{K}L_2)$ and $S = \sin(\sqrt{K}L_2)$. The primary requirement for the point-to-point imaging is $R_{12} = L_1C + (S/\sqrt{K}) - L_1L_3\sqrt{K}S + L_3C = 0$ to eliminate the image blurring contributed by the initial beam divergence. Here $M = R_{11} = C - L_3\sqrt{K}S$ is the magnification factor, which is a key parameter for resolution improvement. The detailed beamline and APL parameters are shown in Table I.

The validity of the imaging lens system (see Fig. 3 with the design parameters shown in Table I) is confirmed by the particle tracking simulation code General Particle Tracer (GPT) [22] and the three-dimensional (3D) particle-in-cell code IBMP [23]. GPT is used to generate the initial particle distribution with the parameters discussed in Sec. II A. An ideal 100% contrast electron beam is

TABLE I. Key parameters of the designed HEER system. The parameters describing the layout of the lens system are defined in Fig. 3.

Parameter	Value (cm)	Parameter	Value
L_1	0.33	MF	20
L_2	3	Fourier plane position	3.6 cm
L_3	41.54	I_{pe}	500 A
Total length	44.87	$\partial B_\theta/\partial r$	400 T/m

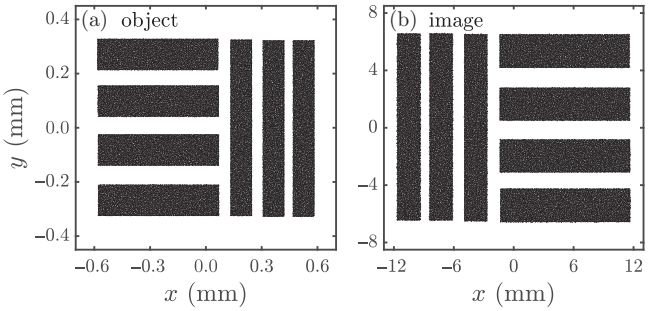

FIG. 4. Simulated results of the strip beam distributions at the object (a) and image (b) planes. The beam energy spread is 0.5%, and the aperture is placed on the Fourier plane with a radius of 4.5 μm.

assumed after the beam transports through the test target, as shown in Fig. 4(a). Then the 3D particle coordinates and velocity distributions are imported into IBMP for the next beamline simulation. After a vacuum drift section of $L_1 = 0.33$ cm, the electron beam with energy of 50 MeV (energy spread of 0.5%) enters into the plasma lens. Focusing is due to the plasma discharge current, which is counter-moving with the beam propagation direction (i.e., z axis). The azimuthal magnetic field B_θ as mentioned above has been modeled in IBMP. Subsequently, the electron beam reaches the Fourier plane, where particles that were scattered to large angles within the object can be removed through the aperture, which can be clearly seen from Fig. 3. Figure 4(b) shows the point-to-point image simulation result with an MF of about 19.9, which is in good agreement with the actual design value illustrated in Table I. The same magnification in both x and y directions has been achieved, which is one of the advantages of this imaging lens system.

For quantitative spatial resolution, here we use more macroparticles to simulate smaller regions while keeping the magnification unchanged. The corresponding strip density n_{be} at the image plane is shown in Fig. 5(a). Detailed measurement of the resolution has been described in Refs. [2] and [5]. The edge spread function (ESF), i.e., the intensity projection on the x axis along the bar indicated by the red rectangular region in Fig. 5(a), can be seen from Fig. 5(b). It is worth noting that the mesh resolution of the beam density distribution in Fig. 5(a) is 0.5 μm, which is comparable to the ultimate HEER resolution limited by the resolution of the yttrium aluminum garnet (YAG) screen and the charge-coupled device (CCD) camera used in the experiments. In addition, the derivative of the ESF and its Gaussian fit are shown in Fig. 5(c), resulting in a fit rms width of 1.1 μm (~2.2 pixels), which is the spatial resolution of this designed HEER system. One thus can expect a better spatial resolution using YAG screens and CCD cameras with higher resolutions. The noise in Figs. 5(b) and 5(c) is due to the relatively small number of macroparticles; however, it is sufficient for quantitative resolution.

III. DISCUSSION

Consistent with conventional focusing systems, the spatial resolution of plasma lens radiography depends strongly on three contributions [3]: chromatic effects, image blur due to multiple Coulomb scattering (MCS), and the resolutions of the YAG screen and the CCD camera used in the experiments.

First, the spatial resolution restricted by chromatic aberrations due to the initial energy spread in combination with the extra energy spread induced by scattering in the object can be expressed [4] as $\Delta x = L_C \varphi \delta$. Here $L_C = T_{126}/M$

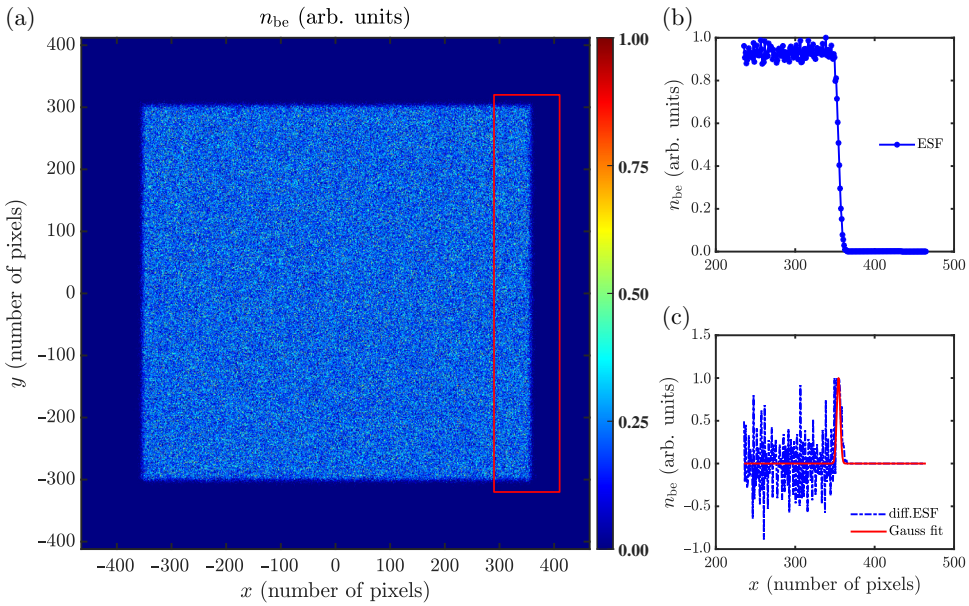

FIG. 5. (a) Distribution of the beam density n_{be} at the image plane, which is normalized to the maximum. (b) The intensity projection on the x axis along the bar indicated by the red rectangular region in panel (a), i.e., edge spread function. (c) Line spread function (i.e., the differential of the intensity projection) and its Gaussian fit (red solid line), indicating a resolution of 1.1 μm (~2.2 pixels) on the image plane. Also, the resolution is limited by the resolutions of the YAG screen and the CCD camera used in the experiments.

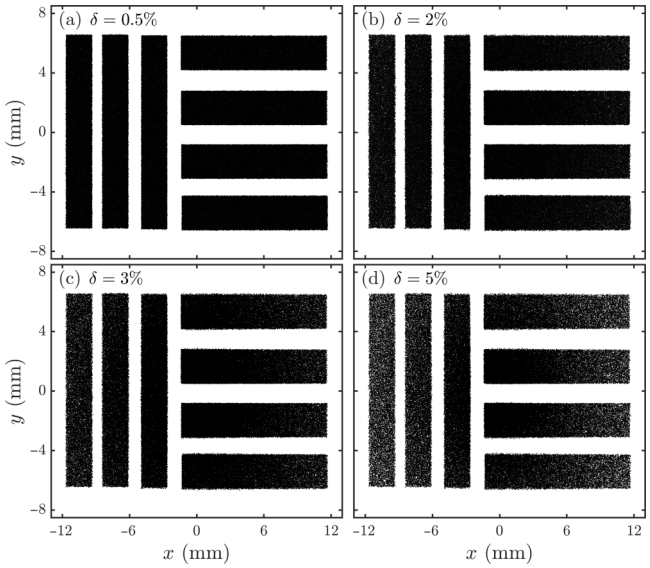

FIG. 6. The transverse projection beam distribution in the image plane with the beam energy spread δ of (a) 0.5%, (b) 2%, (c) 3%, and (d) 5%. The aperture is placed on the Fourier plane with a radius of 4.5 μm.

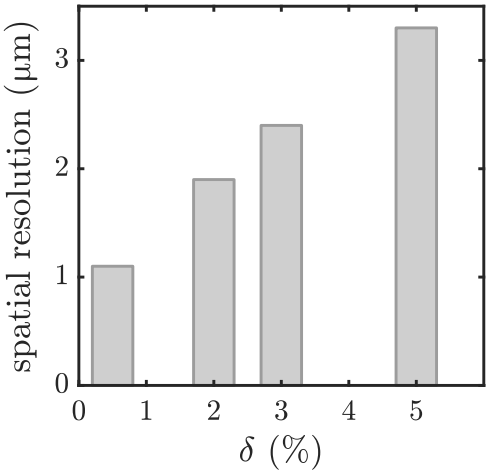

FIG. 7. The variation of the spatial resolution with the increase of the energy spread (from 0.5% to 5%) shown in Fig. 6. The analysis method has been discussed in Sec. II B.

is the chromatic length, with T_{126} the matrix element of the second-order transfer matrix, φ is the deflection angle, and δ is the relative energy deviation. Note that the extra energy spread induced by the object is small compared to the full energy for the high-energy electron beam (50 MeV) and is not included in this work. It should be mentioned that the chromatic dependence of an APL is much weaker than that of the solenoid and quadrupole triplet [12]. On the one hand, solenoid magnets are characterized by a focusing strength $\sim 1/\gamma^2$, resulting in the limitation of applications, which are only suitable for beams in the low-energy sections [24]. On the other hand, quadrupoles focus beam particles in one direction while defocusing them in the orthogonal direction, i.e., the betatron function reaches a large value at the exit of the first quadrupole magnet. Moreover, together with a large quadrupole gradient (up to nearly 600 T/m), the chromatic effects could be increased, which further leads to emittance growth and beam degradation [9,24].

However, in contrast to solenoids and quadrupole magnets, an APL whose focusing strength scales as $1/\gamma$ focuses the beam in both horizontal and vertical directions and can provide adjustable magnetic fields up to 3.6 kT/m [18] within a compact size (a few centimeters). This means that the HEER system based on APLs has a high tolerance for chromatic aberrations.

We then simulate the injected beam with energy spread from 0.5% to 5% to characterize the influence of the chromatic effect on spatial resolution, as shown in Fig. 6 with the transverse projection beam distribution on the image plane. The center part of the images in this figure is clear but the edge part is blurred, which is due to the high-order matrix element from energy spread for larger x-y position. In addition, the variation of the spatial resolution with the increase of the energy spread can be seen from Fig. 7. With the same method as mentioned in Sec. II B, we determined that the resolution in the case of $\delta = 5\%$ [Fig. 6(d)] is about 3.3 μm (with 1 pixel = 0.5 μm), which is close to the level reached by the conventional HEER system with a 1% energy spread and a factor of ∼15 magnification. Therefore, the HEER based on a plasma lens, which has a high tolerance for chromatic aberrations, is suitable for imaging thick target materials.

Another important requirement of a HEER system is the Fourier plane, located between the object and image planes. An aperture placed on the Fourier plane is an essential element of the imaging lens system to enhance the image contrast and obtain higher resolution ability that can be achieved (see Fig. 3). According to the transfer matrix, the position of the Fourier plane in this system is calculated as 2.7 mm behind the APL. As indicated in Fig. 3, the particle position on the Fourier plane relies only on the scattering angle at the object plane, rather than the initial position. This implies that the electron's angle information at the object plane has been translated into position distribution at the Fourier plane [25]. In this way, beam particles that were scattered to large angles by MCS can be removed to form bright-field images.

The length of the aperture, which does not have significant influences on the image, is not included in this work [4]. Moreover, the x and y positions of the Fourier plane are almost at the same position with the assumption of a linear focusing force in this compact symmetric plasma imaging system, which is another advantage of the HEER system based on the APL. With suitable aperture position and radius, pictures with high resolutions can be imaged

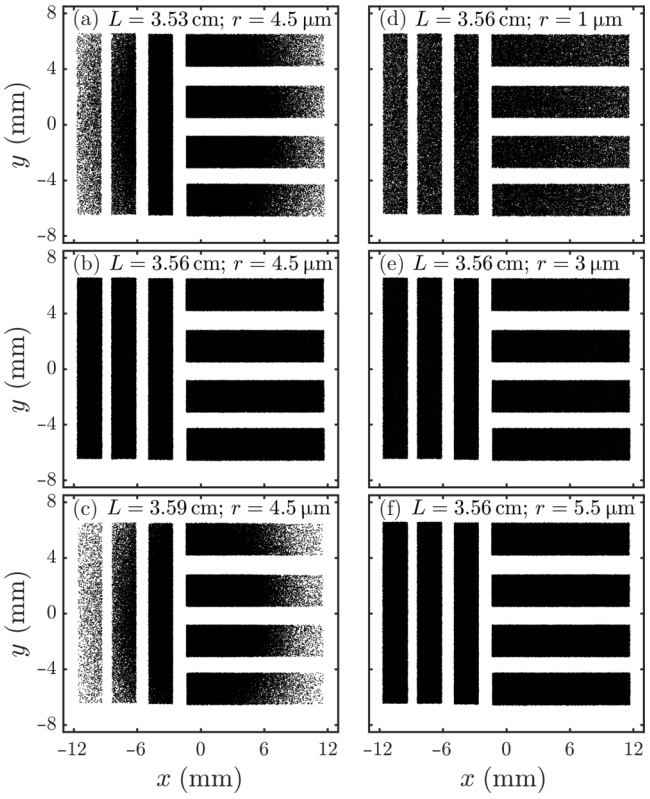

FIG. 8. Simulated images at (a)–(c) different aperture positions L and (d)–(f) different radii r, where $L = 3.56$ cm and $r = 4.5$ μm are the desired aperture position and suitable radius, respectively.

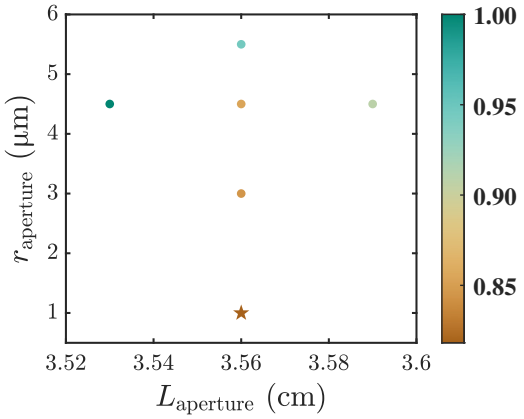

FIG. 9. Spatial resolutions (arbitrary units) at different aperture positions and radii, where the star represents the optimum resolution, at a cost of lowering the final electron intensity reaching the image plane [compare Figs. 8(b) and 8(d)]. It should be noted that the results are normalized to the maximum [in the case of $L = 3.53$ cm and $r = 4.5$ μm, Fig. 8(a)].

by the lens. The aperture is kept at the same position with an identical radius of 4.5 μm in the above simulations.

Next, several simulations have been carried out to characterize the aperture parameters, as can be seen from Fig. 8. The corresponding spatial resolutions in these six cases are shown in Fig. 9, which are normalized to the maximum [in the case of $L = 3.53$ cm, $r = 4.5$ μm, Fig. 8(a)]. Comparing [Figs. 8(a)–8(c)] and Figs. [8(d)–8(f)], a clear picture [see Fig. 8(b)] with 1.1-μm spatial resolution can be imaged by the lens system with desired aperture position and suitable radius. It is worth emphasizing that the image contrast can be further improved by using a smaller aperture [Fig. 8(d)] to obtain a better spatial resolution (the star in Fig. 9), at a cost of lowering the final electron intensity reaching the image plane [compare Figs. 8(b) and 8(d)].

Additionally, the uniformity of the plasma discharge current, which has been measured in experiments [13,18,21], plays an important role in developing the HEER system based on an APL. In previous works, researchers have observed that the magnetic field profile is linear only close to the center axis [24] in a hydrogen-filled capillary discharge waveguide. Great efforts have been carried out in several laboratories to increase the linearity and thus preserve the emittance of the beam, such as by changing from a light gas species to a heavier gas species [18,21], and increasing the plasma temperature and discharge current [13]. As shown in Figs. 6 and 7 of Ref. [18], APLs can remain linear throughout the time and aperture range with the heavy discharge gas of argon even at a very high focusing gradient. For future experimental verification, the proposed plasma imaging lens system will also use argon to preserve the beam emittance.

It is also worth pointing out that the plasma lens system, including background gas, electrons, and ions, is not a vacuum chamber. Together with the beam-plasma parameters, we have considered the Coulomb interaction between the beam electrons and plasma electrons in IBMP. The algorithm uses the Monte Carlo model developed by Nanbu [26,27], which allows for relatively large time steps and weighted particles. Furthermore, our method accounts for relativistic effects [28]. We have performed simulations using the collisional electromagnetic kinetic code EPOCH [29] to cross-check the collisional scheme in IBMP, which shows very good agreement. From the simulation results, the energy loss caused by the Coulomb collision between the beam and background particles is small and can be ignored, also indicating that the plasma lens can be widely used in the HEER system as an excellent imaging lens.

In addition, a compact cascaded HEER system based on PMQs has been verified, and experimental investigations of the feasibility of this system for single-shot high-energy electron imaging with unprecedented micron resolution have been reported [8]. Because of the wider field of view, electromagnetic quadrupole magnets are another choice for the second-stage imaging lens. Therefore, we believe that a multistage HEER system based on APLs and quadrupoles can be achieved. For example, PMQs mounted downstream of the APL, with ultrahigh

gradient, convenience, and cost effectiveness, are the ideal choice to realize such a cascaded system. It is expected to achieve nanometer-level spatial resolution with a larger MF using the two-stage cascade imaging.

IV. CONCLUSION

In conclusion, a novel HEER system consisting of a 50-MeV electron linear accelerator combined with a 3-cm-long capillary to provide an MF of 20 has been proposed. With this system, the distance from the object plane to the imaging plane can be compressed to 45 cm, in contrast to a few meters with MF ~ 10 in the case of conventional focusing systems. The validity of the plasma imaging optics is confirmed by particle tracking simulations using realistic electron beam parameters, through the whole imaging section. These simulation results demonstrate the first plasma-based HEER system with micron-level spatial resolution. The advantages of the plasma imaging system are that it has a high tolerance for chromatic aberrations, is suitable for imaging thick target materials, and has radial symmetric focusing and adjustable focusing gradients.

A more careful start-to-end simulation will be performed, taking into account multiple elastic and inelastic scattering of electrons inside the sample [30]. Future upgrades to this system include the successful implementation of a cascaded HEER system for obtaining a large MF to achieve improved resolving power. In addition, the major challenge of a plasma imaging lens is the small field of view (about 1 mm). For this reason, a He-Ne laser co-propagating with the electron beam should be used to align the sample and the APL to the electron beamline axis. A more compact imaging system based on an APL can be obtained with a higher magnetic gradient of up to a few kiloteslas per meter, and thus the spatial resolution can be further improved with a larger MF.

In addition to the high-resolution imaging of static objects, the HEER system could be used in dynamic experiments with the expected picosecond time resolution using picosecond or even femtosecond electron beams from a state-of-the-art photocathode rf gun (which will be constructed at IMP in the near future), such as visualizing melting processes [10], inertial fusion implosions [31], laser-plasma interactions, and the irradiation damage of nuclear materials. Taking advantage of the ultrashort electron probes, the plasma discharge current (which lasts about a few microseconds in a common APL) can be considered as constant during the transport of the bunch pulses. Thus the plasma-based imaging lens system discussed in this work can also be used in imaging dynamic objects. Moreover, by changing the delay time between plasma ignition and the trigger of the beam pulses, the plasma lens can achieve different MF values. It should be noted here that causes of potential blurring in diagnosing fast dynamic processes are due to synchronization between the rf and laser, repeatability between multiple beam pulses, spatial uniformity, and current intensity.

ACKNOWLEDGMENTS

This work is supported by the National Key Research and Development Program of China (Grant No. 2019YFA0404901), and the National Natural Science Foundation of China (Project No. 12075046).

APPENDIX: BEAM DIVERGENCE AND OFFSET

To determine the influence of the divergence angle on the performance of the plasma-based imaging lens, we assume that the electron beam from the object is coaxial with the capillary. With the beam-plasma parameters and the transfer matrices given in Sec. II, the electron trajectories from the object plane to the Fourier plane can be seen from Fig. 10. Although the divergence angle of the beam electron at $R = 0$ can reach up to ± 24 mrad (see the green dotted line in Fig. 10), we can deduce that the beam electron at $\pm 0.5R$ with an angle larger than ± 18.9 mrad will hit the capillary wall, resulting in beam loss (as illustrated in the black solid lines in Fig. 10). Moreover, only electrons with a divergence angle $\in [-0.2, 0.2]$ mrad can be transported through the aperture with the radius of 4.5 μm, which can be seen from Fig. 10.

As discussed in Sec. III, an electron beam undergoes MCS when passing through the object, and the divergence angle σ_θ can be calculated statistically [32] as

$$\sigma_\theta = \frac{13.6\,\mathrm{MeV}}{\beta cp} Z \sqrt{\frac{x_0}{X_0}} \left[1 + 0.038 \ln\left(\frac{x_0}{X_0}\right)\right], \quad \text{(A1)}$$

which is approximately Gaussian-shaped. Here, p is the beam momentum, βc is the beam velocity, $Z = 1$ is the charge number for electrons, x_0 is the thickness of the static object, and X_0 is the radiation length of the material.

Considering an aluminum target ($X_0 = 8.9$ cm) with thickness $x_0 = 647$ μm, the angular spread that an electron beam with energy of $\varepsilon_0 = 50$ MeV gains by passing

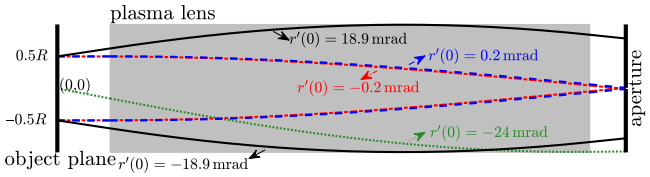

FIG. 10. Electron trajectories from the object plane to the Fourier plane. Beam electrons are set on the object plane with positions 0 and $\pm 0.5R$ and divergence angles of ± 0.2 mrad, ± 18.9 mrad, and -24 mrad. Here, $R = 0.5$ mm is the radius of the capillary, and an aperture is placed on the Fourier plane with a radius of 4.5 μm. It should be noted that the distance from the object plane to the plasma lens is L_1 (given in Table I) and the length of the second vacuum drift section in this figure is 0.27 cm.

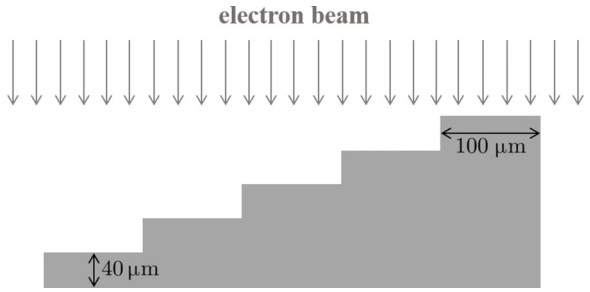

FIG. 11. The aluminum stepwise static target with different thicknesses: 40, 80, 120, 160, and 200 μm. The width of the target is 500 μm. The direction of the electron beam is also shown.

through it is 18.9 mrad. During this stage, up to 99.3% [$= \varepsilon/\varepsilon_0 = \exp(-(x_0/X_0))$, with ε the beam energy after interacting with the target, from Ref. [33]] of the beam energy can be preserved. However, the beam electrons are all removed by the aperture in Fig. 10. With the thickness decreasing to 200 μm, an aperture with a radius of a few hundred microns must be chosen to provide sufficient collecting angle and high image contrast. This can also be applied to estimate the thickness of other targets such as silicon, copper, and gold, which are usually used in experiments. Therefore, we can expect that the plasma-based imaging lens in this work would achieve excellent spatial resolution with appropriate sample targets and aperture.

Together with the changes in divergence angle and energy due to MCS when the electrons pass through the target, an aluminum stepwise static target with different thicknesses can be imaged using APLs. The schematic of the target is shown in Fig. 11, which is easy to build and convenient to use in practice. Such a sample can also satisfy the requirement of areal-density resolution. Moreover, setscrew, mechanical watches, a TEM grid, and copper or gold sample targets have been successfully imaged using conventional focusing systems in experiments [6,30]. High-resolution images of these samples can also be achieved using the plasma lens discussed in this work.

In addition to the electron beam moving along the center axis of the capillary, the beam would also offset from the plasma lens. This results in a lowering of the electron flux reaching the image plane. In this case, the dark-field imaging [5] captured by selecting electrons with large scattering angles can be considered, in contrast to on-axis bright-field imaging. With the help of dark-field imaging, information such as outlines, boundaries, and defects can be obtained. Combining the bright- and dark-field HEER, more detailed imaging could be expected.

Note that the linearity of the focusing field can be guaranteed with the discharge gas of argon and a large discharge current. Therefore, the high-order effects of edge blurring are negligible, resulting in clearer images than that in conventional focusing systems. If the beam offset reaches $0.5R$ ($= 250$ μm) in a certain trigger (i.e., the beam center on the axis of $r = 0.5R$), the beam loss would be considerable and no imaging could be observed on the image plane. According to the diameter and discharge current of the APL, the tolerance for divergence angle and thus the offset can be deduced from the transfer matrices as discussed above. Additionally, at the Fourier plane, scattered electrons are radially sorted by the magnitude of their divergence angle in the object plane, i.e., electrons with larger angles are away from the center axis. Thus a movable and variable-radius aperture is the key to achieving radiography with high spatial resolution by filtering out large-angle (i.e., bright-field imaging) or small-angle (i.e., dark-field imaging) scattered electrons.

[1] N. King *et al.*, An 800-MeV proton radiography facility for dynamic experiments, Nucl. Instrum. Methods Phys. Res., A **424**, 84 (1999).

[2] F. Merrill, F. Harmon, A. Hunt, F. Mariam, K. Morley, C. Morris, A. Saunders, and C. Schwartz, Electron radiography, Nucl. Instrum. Methods Phys. Res., B **261**, 382 (2007).

[3] C. L. Morris, N. S. P. King, K. Kwiatkowski, F. G. Mariam, F. E. Merrill, and A. Saunders, Charged particle radiography, Rep. Prog. Phys. **76**, 046301 (2013).

[4] Q. Zhao, S. Cao, M. Liu, X. Sheng, Y. Wang, Y. Zong, X. Zhang, Y. Jing, R. Cheng, Y. Zhao, Z. Zhang, Y. Du, and W. Gai, High energy electron radiography system design and simulation study of beam angle-position correlation and aperture effect on the images, Nucl. Instrum. Methods Phys. Res., A **832**, 144 (2016).

[5] Z. Zhou, Y. Du, S. Cao, Z. Zhang, W. Huang, H. Chen, R. Cheng, Z. Chi, M. Liu, X. Su, C. Tang, Q. Tian, W. Wang, Y. Wang, J. Xiao, L. Yan, Q. Zhao, Y. Zhu, Y. Zhou, Y. Zong, and W. Gai, Experiments on bright-field and dark-field high-energy electron imaging with thick target material, Phys. Rev. Accel. Beams **21**, 074701 (2018).

[6] F. E. Merrill, J. Goett, J. W. Gibbs, S. D. Imhoff, F. G. Mariam, C. L. Morris, L. P. Neukirch, J. Perry, D. Poulson, R. Simpson, P. L. Volegov, P. L. Walstrom, C. H. Wilde, C. Hast, K. Jobe, T. Smith, U. Wienands, A. J. Clarke, and D. Tourret, Demonstration of transmission high energy electron microscopy, Appl. Phys. Lett. **112**, 144103 (2018).

[7] Z. Ran, Z. Li, Q. Zhao, X. Shen, Y. Zong, Z. Zhang, Y. Zhou, M. Liu, R. Xiao, J. Li, and S. Cao, Demonstration of high energy electron radiography with sub-micron spatial resolution, Nucl. Instrum. Methods Phys. Res., A **1015**, 165769 (2021).

[8] Z. Zhou, Y. Fang, H. Chen, Y. Wu, Y. Du, L. Yan, C. Tang, and W. Huang, Demonstration of single-shot high-quality cascaded high-energy-electron radiography using compact imaging lenses based on permanent-magnet quadrupoles, Phys. Rev. Appl. **11**, 034068 (2019).

[9] D. Xiang, F. Fu, J. Zhang, X. Huang, L. Wang, X. Wang, and W. Wan, Accelerator-based single-shot ultrafast transmission electron microscope with picosecond

temporal resolution and nanometer spatial resolution, Nucl. Instrum. Methods Phys. Res., A **759**, 74 (2014).

[10] Z. Zhou, Y. Fang, H. Chen, Y. Wu, Y. Du, Z. Zhang, Y. Zhao, M. Li, C. Tang, and W. Huang, Visualizing the melting processes in ultrashort intense laser triggered gold mesh with high energy electron radiography, Matter Radiat. Extremes **4**, 065402 (2019).

[11] R. Weingartner, M. Fuchs, A. Popp, S. Raith, S. Becker, S. Chou, M. Heigoldt, K. Khrennikov, J. Wenz, T. Seggebrock, B. Zeitler, Z. Major, J. Osterhoff, F. Krausz, S. Karsch, and F. Grüner, Imaging laser-wakefield-accelerated electrons using miniature magnetic quadrupole lenses, Phys. Rev. ST Accel. Beams **14**, 052801 (2011).

[12] J. van Tilborg, S. Steinke, C. G. R. Geddes, N. H. Matlis, B. H. Shaw, A. J. Gonsalves, J. V. Huijts, K. Nakamura, J. Daniels, C. B. Schroeder, C. Benedetti, E. Esarey, S. S. Bulanov, N. A. Bobrova, P. V. Sasorov, and W. P. Leemans, Active Plasma Lensing for Relativistic Laser-Plasma-Accelerated Electron Beams, Phys. Rev. Lett. **115**, 184802 (2015).

[13] R. Pompili *et al.*, Focusing of High-Brightness Electron Beams with Active-Plasma Lenses, Phys. Rev. Lett. **121**, 174801 (2018).

[14] A. Marocchino *et al.*, Experimental characterization of the effects induced by passive plasma lens on high brightness electron bunches, Appl. Phys. Lett. **111**, 184101 (2017).

[15] C. E. Doss, E. Adli, R. Ariniello, J. Cary, S. Corde, B. Hidding, M. J. Hogan, K. Hunt-Stone, C. Joshi, K. A. Marsh, J. B. Rosenzweig, N. Vafaei-Najafabadi, V. Yakimenko, and M. Litos, Laser-ionized, beam-driven, underdense, passive thin plasma lens, Phys. Rev. Accel. Beams **22**, 111001 (2019).

[16] J. J. Su, T. Katsouleas, J. M. Dawson, and R. Fedele, Plasma lenses for focusing particle beams, Phys. Rev. A **41**, 3321 (1990).

[17] T. Barklow *et al.*, Beam delivery and beamstrahlung considerations for ultra-high energy linear colliders, J. Instrum. **18**, P09022 (2023).

[18] K. N. Sjobak, E. Adli, R. Corsini, W. Farabolini, G. Boyle, C. A. Lindstrøm, M. Meisel, J. Osterhoff, J.-H. Röckemann, L. Schaper, and A. E. Dyson, Strong focusing gradient in a linear active plasma lens, Phys. Rev. Accel. Beams **24**, 121306 (2021).

[19] J.-J. Lan, Z.-H. Hu, Z.-H. Ran, J. Li, Y.-W. Zhou, S.-C. Cao, R. Cheng, Y.-H. Chen, W.-B. Yan, Q.-T. Zhao, Y.-T. Zhao, Z.-M. Zhang, and Y.-N. Wang, Experimental observation of the electron beam focusing effect induced by plasma currents with opposite directions, Phys. Rev. E **108**, 065203 (2023).

[20] L. Serafini and J. B. Rosenzweig, Envelope analysis of intense relativistic quasilaminar beams in rf photoinjectors: mA theory of emittance compensation, Phys. Rev. E **55**, 7565 (1997).

[21] C. A. Lindstrøm, E. Adli, G. Boyle, R. Corsini, A. E. Dyson, W. Farabolini, S. M. Hooker, M. Meisel, J. Osterhoff, J.-H. Röckemann, L. Schaper, and K. N. Sjobak, Emittance Preservation in an Aberration-Free Active Plasma Lens, Phys. Rev. Lett. **121**, 194801 (2018).

[22] Pulsar Physics; the General Particle Tracer (GPT) code; https://www.pulsar.nl/gpt/.

[23] Z.-H. Hu and Y.-N. Wang, Hollow structure formation of intense ion beams with sharp edge in background plasmas, Phys. Plasmas **23**, 023103 (2016).

[24] E. Chiadroni *et al.*, Overview of plasma lens experiments and recent results at SPARC_LAB, Nucl. Instrum. Methods Phys. Res., A **909**, 16 (2018).

[25] C. Xiao, Z. Xu, H. Lu, J. Liu, C. Xie, Y. Zhao, Y. Geng, S. Huang, S. Zhao, J. Zhu, M. Lai, H. Zhang, H. Zhuo, C. Zhou, and X. Yan, Design of a compact electron radiography system with electron source from laser wakefield accelerator, AIP Adv. **11**, 045030 (2021).

[26] K. Nanbu, Theory of cumulative small-angle collisions in plasmas, Phys. Rev. E **55**, 4642 (1997).

[27] K. Nanbu and S. Yonemura, Weighted particles in Coulomb collision simulations based on the theory of a cumulative scattering angle, J. Comput. Phys. **145**, 639 (1998).

[28] F. Pérez, L. Gremillet, A. Decoster, M. Drouin, and E. Lefebvre, Improved modeling of relativistic collisions and collisional ionization in particle-in-cell codes, Phys. Plasmas **19**, 083104 (2012).

[29] T. D. Arber, K. Bennett, C. S. Brady, A. Lawrence-Douglas, M. G. Ramsay, N. J. Sircombe, P. Gillies, R. G. Evans, H. Schmitz, A. R. Bell, and C. P. Ridgers, Contemporary particle-in-cell approach to laser-plasma modelling, Plasma Phys. Control. Fusion **57**, 113001 (2015).

[30] D. Cesar, J. Maxson, P. Musumeci, Y. Sun, J. Harrison, P. Frigola, F. H. O'Shea, H. To, D. Alesini, and R. K. Li, Demonstration of Single-Shot Picosecond Time-Resolved MeV Electron Imaging using a Compact Permanent Magnet Quadrupole Based Lens, Phys. Rev. Lett. **117**, 024801 (2016).

[31] J. R. Rygg, F. H. Séguin, C. K. Li, J. A. Frenje, M. J.-E. Manuel, R. D. Petrasso, R. Betti, J. A. Delettrez, O. V. Gotchev, J. P. Knauer, D. D. Meyerhofer, F. J. Marshall, C. Stoeckl, and W. Theobald, Proton radiography of inertial fusion implosions, Science **319**, 1223 (2008).

[32] M. C. Thompson, H. Badakov, J. B. Rosenzweig, G. Travish, N. Barov, P. Piot, R. Fliller, G. M. Kazakevich, J. Santucci, J. Li, and R. Tikhoplav, Observations of low-aberration plasma lens focusing of relativistic electron beams at the underdense threshold, Phys. Plasmas **17**, 073105 (2010).

[33] H. A. Bethe and W. H. Heitler, On the stopping of fast particles and on the creation of positive electrons, Proc. Math. Phys. Eng. Sci. **146**, 83 (1934).